

ISOTOPIC SEPARATION

Barely porous organic cages for hydrogen isotope separation

Ming Liu¹, Linda Zhang², Marc A. Little¹, Venkat Kapil³, Michele Ceriotti³, Siyuan Yang⁴, Lifeng Ding⁴, Daniel L. Holden¹, Rafael Balderas-Xicohtencatl², Donglin He¹, Rob Clowes¹, Samantha Y. Chong¹, Gisela Schütz², Linjiang Chen^{1,5}, Michael Hirscher^{2*}, Andrew I. Cooper^{1,5*}

The separation of hydrogen isotopes for applications such as nuclear fusion is a major challenge. Current technologies are energy intensive and inefficient. Nanoporous materials have the potential to separate hydrogen isotopes by kinetic quantum sieving, but high separation selectivity tends to correlate with low adsorption capacity, which can prohibit process scale-up. In this study, we use organic synthesis to modify the internal cavities of cage molecules to produce hybrid materials that are excellent quantum sieves. By combining small-pore and large-pore cages together in a single solid, we produce a material with optimal separation performance that combines an excellent deuterium/hydrogen selectivity (8.0) with a high deuterium uptake (4.7 millimoles per gram).

Deuterium (D) is used as a neutron moderator, as a nonradioactive isotopic tracer, and in neutron scattering experiments. These applications need high-purity deuterium, which is expensive because of its low natural abundance (0.0156 mol %). Typically, D₂ is produced by electrolysis of heavy water and extracted through the Girdler-sulfide process (1) or by cryogenic distillation at 24 K (2). Both processes are costly and energy intensive because of the multiple enrichment steps required (3).

An attractive alternative to purify D₂ from H₂/D₂ gas mixtures is to adsorb D₂ selectively on a microporous bed (4). Kinetic quantum sieving (KQS) with nanoporous solids was first proposed by Beenakker *et al.* (5). The KQS effect becomes pronounced when the difference in size between a hydrogen molecule and the confining space is comparable to the thermal de Broglie wavelength of molecular hydrogen, $\lambda_T = h/(2\pi m k_B T)^{1/2}$ (h , Planck's constant; m , mass; k_B , Boltzmann constant; T , temperature). Quantum sieving has been exploited for the separation of gaseous isotope mixtures such as D₂/H₂ (6), but it is challenging to identify suitable porous solids. This is because KQS requires ultrafine pore apertures (~3 Å) (7, 8), and this typically leads to materials with low pore volumes and, hence, low D₂ adsorption capacities, making such processes difficult to scale. An

analogous selectivity-capacity trade-off—or, for membranes, a selectivity-permeance trade-off—is observed for a wide range of other gas separations that do not involve KQS (9–12).

Various porous materials have been studied for hydrogen isotope separation, including carbons (13, 14), carbon nanotubes (15), zeolites (16, 17), metal-organic frameworks (MOFs) (6, 18, 19), covalent organic frameworks (COFs) (20), and 2D crystals (21). MOFs and COFs have received much attention because of their crystalline nature and synthetically tunable pore size and functionality (22). However, even with MOFs or COFs, it is challenging to tune pore sizes at the exceptionally fine level required for KQS. For example, in MOFs, a common strategy for tuning the pore apertures is through systematic expansion or reduction of the number of the phenylene rings in the organic linker, with an increment or a decrement of ~2.8 Å (23); that is, too coarse for fine-tuning the aperture for optimum KQS.

Porous organic cages (POCs) (24, 25) are discrete molecules that have been used previously for the separation of xylene isomers (26), noble gases (27), and chiral molecules (27). POCs might also be promising candidates for H₂/D₂ separation but, unlike MOFs and COFs, it is difficult to tune the pore size in POCs simply by changing the constituent linkers. Because POCs are discrete molecules, small changes in their molecular structure can have profound effects on the solid-state packing of the cages and, hence, the pore structure (24). Modifying only the interior of the cage molecule, rather than the cage structure itself, could allow us to avoid altering the crystal packing. Internal functionalization is possible. For example, Mastalerz and co-workers described the postsynthetic modification of the interior of organic cages by using a sixfold Williamson etherification (28), but this interior modification affected the cage shape, which in turn altered the crystal packing mode.

Systematically tuning the pore size of organic cages by postsynthetic modification

We synthesized a series of internally post-functionalized porous organic cages that crystallized in an isostructural way. Specifically, we used a protection-deprotection strategy to produce cages where five out of the six internal reaction sites in the cage cavity were functionalized by means of a formaldehyde “tying” method we reported previously (29) (Fig. 1, A and B). After deprotection, the single unreacted diamine group can be reacted with a range of aldehyde or ketone precursors to achieve ultrafine control over the cage cavity size and, hence, the pore envelope (Fig. 1C). This method allowed us to tune the size and shape of the cage pore systematically at the atomic level without affecting the external cage shape and size or its crystal packing. Using this strategy, we tuned the pore size for the series of POCs in the range 1.95 to 3.5 Å, which is a useful cut-off range for the separation of gas pairs such as H₂/N₂, H₂/CO, CH₄/N₂, and Xe/Kr (7).

Previously, we reported that an organic cage with six diamine groups, **RCC3**, reacts with six formaldehyde molecules to form **6FT-RCC3** through the formation of cyclic amination rings (29). **RCC3** was reacted with six equivalents of acetaldehyde to form a new cage, **6ET-RCC3** (reaction *a*, Fig. 1B), where bulkier ethylidene bridges replaced the six methylene bridges in **6FT-RCC3**. By contrast, **RCC3** reacted with just a single acetone molecule to form **1AT-RCC3** (29) (reaction *b*, Fig. 1B); steric hindrance prevented further reaction in the cage cavity.

On the basis of this result, we developed a protection-deprotection strategy in which we reacted the five unfunctionalized diamine groups in **1AT-RCC3** with gaseous formaldehyde in the solid state, through a single-crystal-to-single-crystal reaction, to form a new dual “tied” cage molecule, **1AT-5FT-RCC3** (reaction *d*, Fig. 1B and fig. S1). Solid-state synthesis was essential, in that when **1AT-RCC3** was mixed with formaldehyde in solution (CHCl₃ or MeOH), the single acetone protecting group was displaced to afford **6FT-RCC3** (reaction *c* in Fig. 1B and fig. S2). By exploiting the different chemical labilities of imidazolidine rings in **1AT-5FT-RCC3**, we could selectively hydrolyze the single propyl “tie” by stirring in CHCl₃/MeOH (1:1, v/v), thus synthesizing a new deprotected cage, **5FT-RCC3** (reaction *e* in Fig. 1B and fig. S3). After deprotection, we reacted the now vacant diamine group in **5FT-RCC3** with acetaldehyde and propionaldehyde to synthesize two new cages, **1ET-5FT-RCC3** and **1PT-5FT-RCC3** (reaction *f*, Fig. 1B). All reactions proceeded with nearly 100% conversion with no additional purification steps.

The parent cage for this study, **RCC3**, is derived from the shape-persistent imine precursor, **CC3**, which crystallized from most organic solvents to form a microporous solid

¹Materials Innovation Factory and Department of Chemistry, University of Liverpool, 51 Oxford Street, Liverpool, L7 3NY, UK. ²Max Planck Institute for Intelligent Systems, Heisenbergstr. 3, 70569 Stuttgart, Germany. ³Laboratory of Computational Science and Modeling, Institute of Materials, École Polytechnique Fédérale de Lausanne, 1015 Lausanne, Switzerland. ⁴Department of Chemistry, Xi'an JiaoTong-Liverpool University, 111 Ren'ai Road, Suzhou Dushu Lake Higher Education Town, Jiangsu Province, 215123, China. ⁵Leverhulme Research Centre for Functional Materials Design, Materials Innovation Factory and Department of Chemistry, University of Liverpool, 51 Oxford Street, Liverpool, L7 3NY, UK.

*Corresponding author. Email: aicooper@liverpool.ac.uk (A.I.C.); hirscher@is.mpg.de (M.H.)

with a diamondoid pore network (24, 26, 27). For guest molecules to diffuse through this pore network, they must pass through the intrinsic cage cavities that act as the tetrahedral nodes (25). Hence, internal functionalization of the cage cavities provided a route to systematically fine-tune pore size without altering the underlying shape and crystallization habit of the cage molecule (30). All cages were isostructural with **CC3**, as determined by powder x-ray diffraction (fig. S4) and single-crystal x-ray diffraction (fig. S5 and table S1). The high crystallographic symmetry of the structures (cubic $F4_32$) did not allow us to determine whether the different tied groups were ordered in the microporous pore structures, but all cages had the same diamondoid pore structure.

To allow for the effect of molecular flexibility on the diffusivity of small gas molecules through these structures, we used molecular dynamics (MD) simulations to calculate a time-averaged pore-limiting envelope (PLE) (27) rather than measuring a single, static pore diameter. These calculations showed that post-

synthetic modification allowed the PLE to range from 1.95 Å (**6ET-RCC3**) to 3.50 Å (**6FT-RCC3**), resulting in a tunability window of 1.55 Å (Fig. 1C). For context, this tunability window equates to the van der Waals (vdW) radius of a single nitrogen atom across the whole series of isostructural cages.

We studied the gas adsorption properties of these cages for four different gases (Fig. 1D). As expected, there is a positive correlation between the cage cavity volume and the overall gas uptake, especially under conditions in which gases are close to saturation (e.g., N_2 at 77 K; orange bars in Fig. 1D). For example, **5FT-RCC3**, with the largest cage cavity in this series, showed the highest uptakes for all four of the gases studied. By contrast, **1AT-5FT-RCC3** showed much lower gas uptakes, and **6ET-RCC3** size-excluded krypton (Kr) and xenon (Xe) altogether.

This synthetic strategy was also used to tune gas selectivity for hard-to-separate gas pairs, such as Xe and Kr (31, 32). Xenon is heavier and more polarizable than Kr, and it tends to

form stronger vdW interactions with most sorbents unless the pores are specifically attuned for Kr adsorption. Preferential Kr adsorption is very rare. For example, just one MOF, **FMOFCu**, adsorbs Kr selectively over Xe at temperatures below 0°C (32).

Most of these organic cages also exhibit higher uptakes for Xe than for Kr, but **1AT-5FT-RCC3** exhibited reverse uptake for these two gases. As shown in fig. S6, the estimated ideal Kr/Xe molar selectivity could be switched below 0°C. We ascribe this effect to **1AT-5FT-RCC3** having a cavity ideally suited to accommodate Kr but too small for Xe. Inserting one additional methyl group to form **6ET-RCC3** rendered the cavity too small to allow adsorption of either gas.

Hydrogen isotope separation using an ultrafine aperture cage

Efficient KQS requires porous solids in which the difference between aperture size and gas diameter is comparable to the de Broglie wavelength. The kinetic diameter of hydrogen is

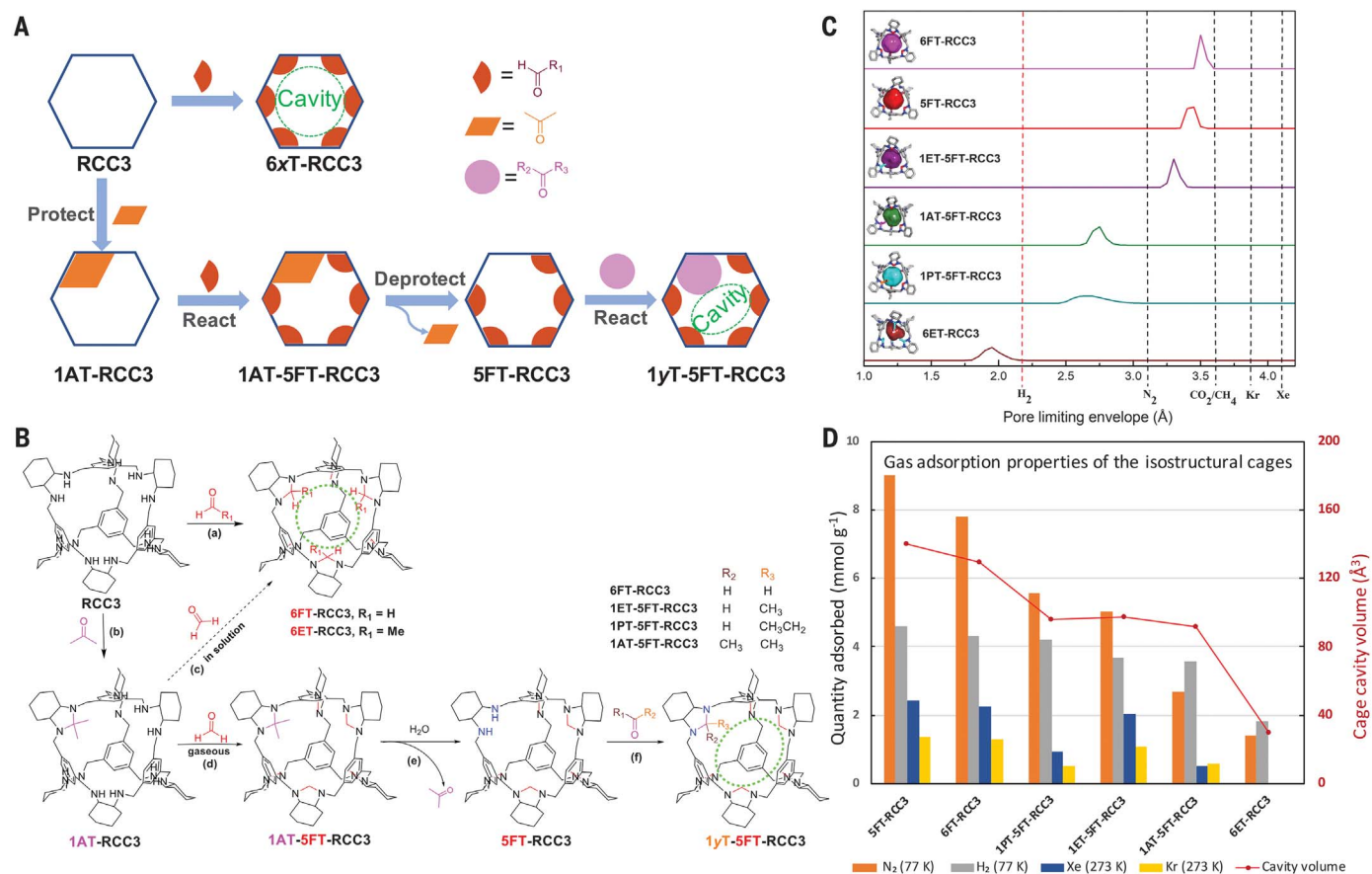


Fig. 1. Fine-tuning pore size by molecular organic synthesis. (A) Scheme showing the protect-functionalize-deprotect strategy for internal cage cavity modification. (B) Full synthesis route for the modified cages, corresponding to the scheme in (A). **FT**, **AT**, **ET**, and **PT** represent products in which the diamine group(s) were tied with formaldehyde, acetone, ethanal (acetaldehyde), and propionaldehyde, respectively; *x* and *y* represent different possible tying groups

(*x* = **E**, **F**; *y* = **A**, **E**, **P**). (C) Representative single-crystal structures of the modified cages showing accessible cavities (colored), along with calculated PLEs for each system. (D) Summary of gas adsorption properties for a range of gases (histogram; left axis) and cage cavity volumes (right axis) of a single modified cage, as calculated by the VOIDOO program on the basis of their crystal structures (probe radius = 2.0 Å) (43).

2.89 Å, and previous studies suggest that the optimum aperture size to achieve QKS with rigid frameworks lies below 3.40 Å (20). It is difficult to obtain porous materials with pore apertures in this range, and so far, only one material with pore size <3.00 Å has been reported to separate D₂ and H₂ (6).

MD simulations suggested that **6ET-RCC3** has a PLE centered at 1.95 Å but with a relatively broad time-averaged size distribution, with a value near the minimum molecular dimension of H₂ (2.2 Å; Fig. 1C) (27). Hydrogen adsorption isotherms obtained from **6ET-RCC3** exhibited hysteresis between 30 and 60 K (Fig. 2B). The H₂ uptake reached a maximum at 50 K (4.8 mmol/g at 1 bar). We observed the same phenomena for D₂ adsorption (figs. S7 and S8). The hysteresis was largest at 30 K and decreased with increasing temperature, suggesting greater equilibration.

We also compared the H₂ adsorption behavior for two other organic cages, **CC3** (24) and **6FT-RCC3**, with calculated pore envelopes of around 4.5 and 3.4 Å, respectively. Both **CC3** and **6FT-RCC3** exhibited reversible type I adsorption isotherms (fig. S9), typical of nanoporous materials without kinetic diffusion barriers. The two cages showed an increased H₂ uptake with decreasing temperature, with maximum uptakes at 30 K of 8.0 and 8.2 mmol/g at 1 bar. Unlike **6ET-RCC3**, no hysteresis was observed for **CC3** or **6FT-RCC3**. This difference suggests that the methyl groups in the **6ET-RCC3** cavities were responsible for its temperature-dependent flexibility, as this is the only structural difference between **6FT-RCC3** and **6ET-RCC3**.

Cryogenic thermal desorption spectroscopy (TDS) measurements verified the hydrogen isotope separation performance of **6ET-RCC3**. H₂ and D₂ desorption rates of **6ET-RCC3** (Fig. 2C) were collected during heating under vacuum with a rate of 0.1 K/s, after prior exposure to a 1:1 H₂/D₂ mixture (10 mbar) at various exposure temperatures (T_{exp}) between 30 and 77 K for 10 min of exposure time (t_{exp}). The area under the desorption peak is proportional to the amount of the desorbing gas; hence, the selectivity for D₂ over H₂ could be obtained from the ratio of the peak areas (6).

TDS measurements showed that the uptake in **6ET-RCC3** increased with increasing temperature until a maximum for H₂ and D₂ was reached at T_{exp} of 60 K before decreasing again at 77 K. The selectivity, $S_{\text{D}_2/\text{H}_2}$, decreased with increasing T_{exp} and exhibited a maximum of 3.9 at 30 K, which is a fairly good separation performance compared with previous reports of QKS (6, 33). The onset temperature of gas desorption is nearly identical to the exposure temperature, because after exposure the chamber is evacuated at T_{exp} before cooling to 20 K. No desorption peak was observed above 60 K for $T_{\text{exp}} = 30$ K, implying no deep penetration

into the structure at this temperature. For higher T_{exp} , the desorption spectra were unusually shifted to higher temperatures, which we attributed to an increased penetration depth of gas molecules into the cage structure. In agreement with observations from

pure gas isotherms, the properties of **6ET-RCC3** can be attributed to the temperature-dependent opening of the pore aperture. This behavior is similar to that observed in MFU-4 reported previously (6), which exhibited different effective aperture sizes at different T_{exp} .

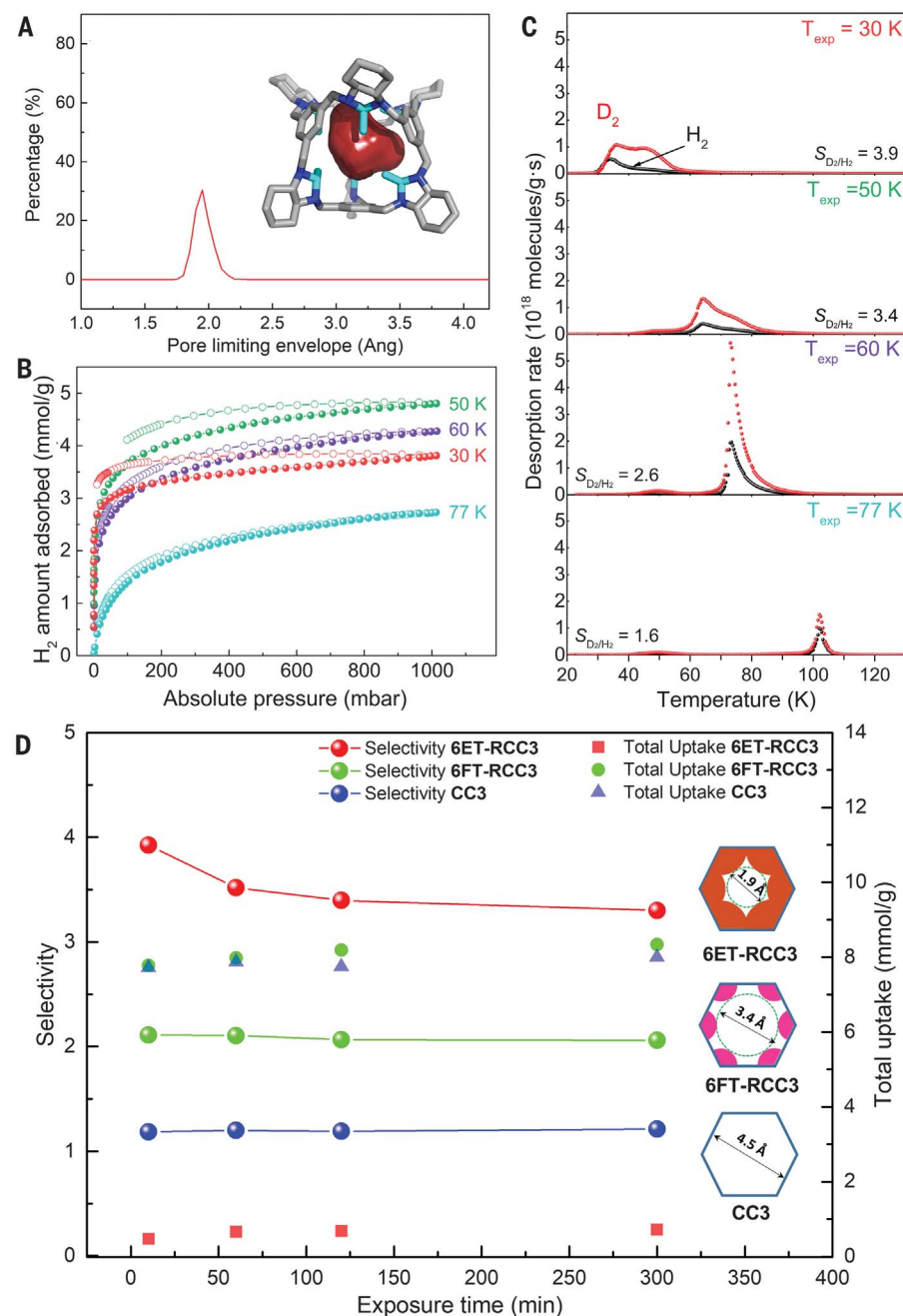


Fig. 2. Kinetic quantum sieving with ultrasmall-pore organic cages. (A) PLE for **6ET-RCC3**. The inset image shows the single-crystal structure of **6ET-RCC3** with its accessible cage cavity (colored). Ang, angstroms. (B) Hydrogen adsorption (solid symbols) and desorption (open symbols) isotherms of **6ET-RCC3** at different temperatures. (C) TDS spectra of **6ET-RCC3** obtained after exposure to a 10-mbar 1:1 D₂/H₂ isotope mixture at different exposure temperatures for a fixed exposure time (t_{exp}) of 10 min. The desorption spectra after evacuation at exposure temperature were measured for a heating rate of 0.1 K/s. (D) D₂/H₂ selectivities and gas uptakes as a function of exposure time at 30 K for **CC3**, **6FT-RCC3**, and **6ET-RCC3**; see supplementary materials for additional comparison (figs. S10 and S11).

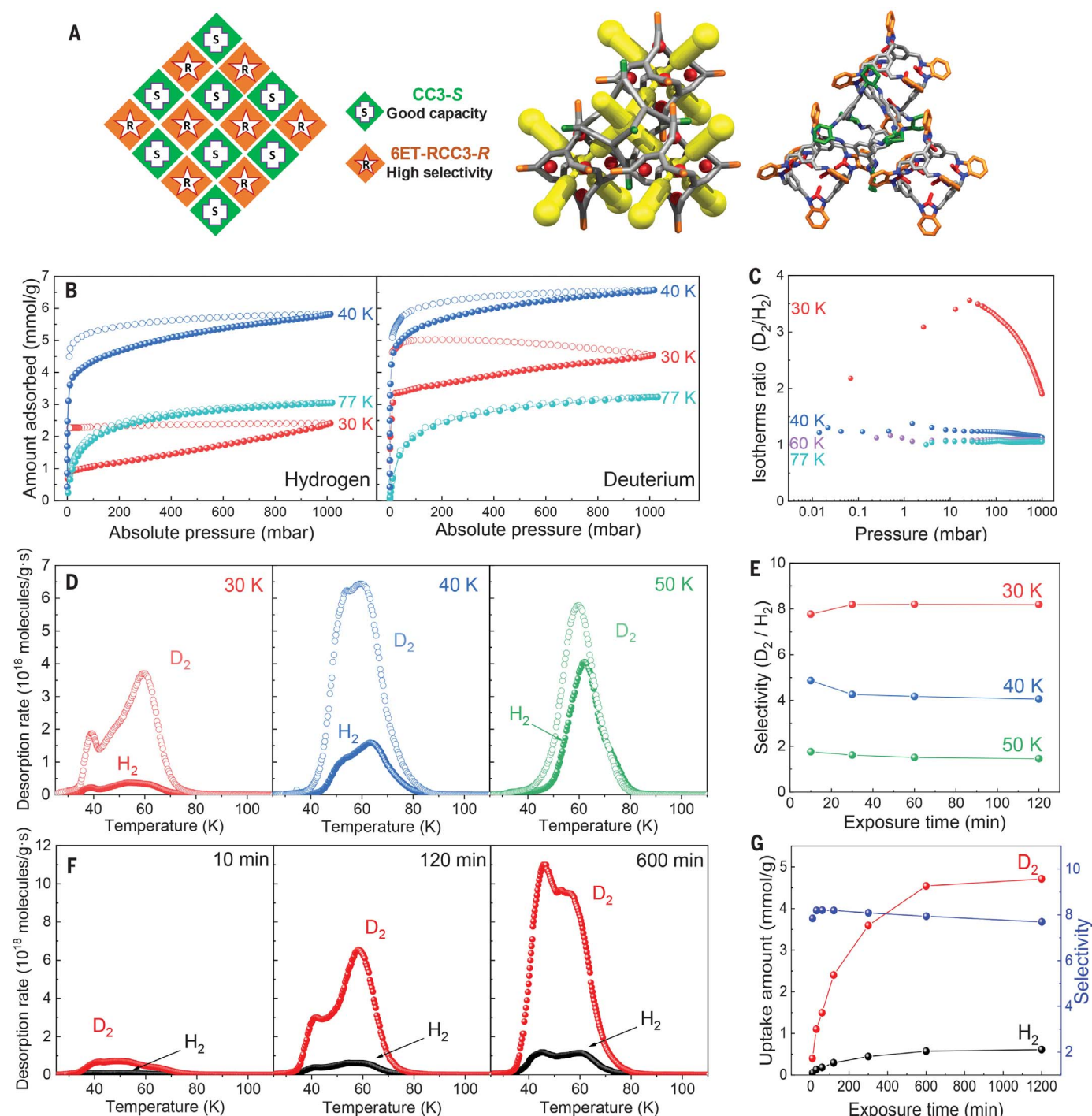


Fig. 3. Formation of a cocrystal enhances the D_2/H_2 separation performance.

(A) (Left) Scheme showing the cocrystal, **Cocryst1**, formed by chiral recognition between two cages to integrate capacity and selectivity in a single material. (Middle) Simplified representation of the crystal structure of **Cocryst1**, with pore channels shown in yellow. (Right) Single-crystal structure of **Cocryst1**. (B) H_2 and D_2 adsorption (closed symbols) and desorption (open symbols) isotherms of **Cocryst1** at different temperatures. (C) D_2/H_2 isotherm ratio as a function of pressure for different temperatures. (D) TDS spectra for **Cocryst1**, obtained after exposure to a 10-mbar 1:1 H_2/D_2 isotope mixture for different exposure temperatures (T_{exp}) and a fixed exposure time (t_{exp}) of 30 min. (E) D_2/H_2 selectivity as a function of t_{exp} at 30 K (red), 40 K (blue), and 50 K (green). (F) TDS spectra for **Cocryst1**, obtained after exposure to a 10-mbar 1:1 H_2/D_2 isotope mixture for different exposure times at 30 K. (G) The corresponding amount of adsorbed H_2 (black) and D_2 (red) and selectivity (blue) as functions of t_{exp} at 30 K.

(D) TDS spectra for **Cocryst1**, obtained after exposure to a 10-mbar 1:1 H_2/D_2 isotope mixture for different exposure temperatures (T_{exp}) and a fixed exposure time (t_{exp}) of 30 min. (E) D_2/H_2 selectivity as a function of t_{exp} at 30 K (red), 40 K (blue), and 50 K (green). (F) TDS spectra for **Cocryst1**, obtained after exposure to a 10-mbar 1:1 H_2/D_2 isotope mixture for different exposure times at 30 K. (G) The corresponding amount of adsorbed H_2 (black) and D_2 (red) and selectivity (blue) as functions of t_{exp} at 30 K.

This flexibility enhanced the access of the isotope molecules to the pores at higher exposure temperatures.

Figure 2D shows S_{D_2/H_2} and the total quantity of gas adsorbed for **6ET-RCC3**, **6FT-RCC3**, and **CC3** as a function of t_{exp} at $T_{\text{exp}} = 30$ K (for detailed TDS spectra, see table S2). **6ET-RCC3** showed an increase in uptake for longer t_{exp} , revealing that diffusion was hindered. At 30 K, S_{D_2/H_2} decreased with longer t_{exp} , from 3.9 to 3.3 between 10 and 300 min of exposure, which is a typical KQS response. The KQS effect is based on the diffusion limitation of the lighter isotope; equilibrium is approached for both isotopes for longer exposure times. The total uptake for **6ET-RCC3** at 30 K was only 0.8 mmol/g at t_{exp} of 300 min, which is related to the hysteresis observed in the isotherm experiment at 30 K. The total gas uptake obtained at 30 K for **CC3** and **6FT-RCC3** was much higher (8.0 mmol/g), consistent with the adsorption results (fig. S8). For the larger-pore materials, **CC3** and **6FT-RCC3**, S_{D_2/H_2} was lower and remained constant at 1.2 and 2.1, respectively, for different t_{exp} , in keeping with rapid, barrier-free diffusion of H_2 and D_2 .

Enhanced quantum sieving performance in a two-component cage cocrystal

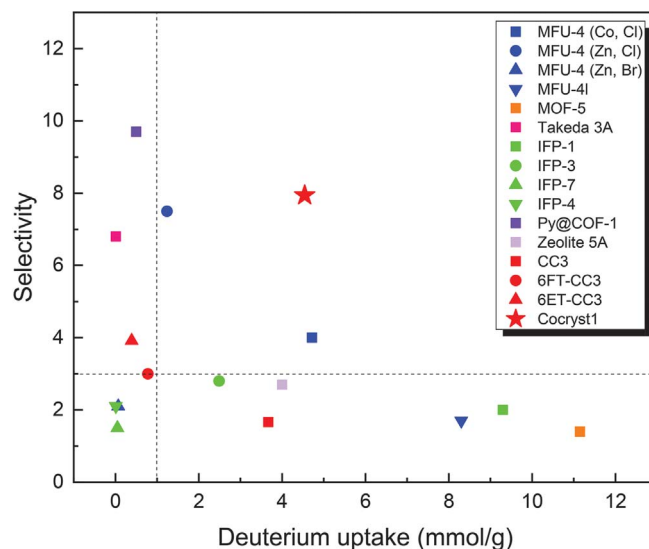
These single-component cage crystals exhibited either good selectivity but poor gas capacity (**6ET-RCC3**) or good gas capacity but poor selectivity (**CC3** and **6FT-RCC3**). For the optimal separation of isotopes, the ideal KQS material should combine large cavities to store more D_2 along with a narrow pore aperture to increase the kinetic separation. Taking advantage of the chiral recognition assembly of discrete cage molecules (34), we designed a cocrystal structure that combined two different cages: **6ET-RCC3** was chosen as the diffusion barrier, blocking H_2 diffusion and providing the KQS effect, and **CC3** was chosen as the partner cage to provide enough pore space for high gas adsorption (Fig. 3A).

The structure of the cocrystal, **Cocryst1** (**6ET-RCC3-R/CC3-S**, 1:1), is shown in Fig. 3A (at right; see fig. S12 for structural details). Because the cage cavities formed the nodes of the diamondoid pore network, four selective **6ET-RCC3** cages surrounded each **CC3** storage. Gas molecules diffusing through the cocrystal were forced to traverse the small pores in **6ET-RCC3**.

Cocryst1 was studied using D_2 and H_2 high-resolution adsorption experiments collected between 20 and 77 K (Fig. 3B; additional isotherms are in fig. S13). The amount of gas adsorbed at 1 bar showed a maximum at 40 K for both gases. As for **6ET-RCC3**, the hysteresis in **Cocryst1** was high at lower temperatures because of the large diffusion barrier, particularly at 30 K; at higher temperatures, a temperature-

Fig. 4. Summary of hydrogen isotope KQS selectivities and adsorption capacities for various porous materials (directly measured by TDS). The list includes carbon [Takeda 3A (44)], MOFs [MFU-4 (6, 22, 44), MOF-5 (44), and IFP (45)], COFs [Py@COF-1 (46)], zeolite 5A (16), and porous organic cages (**CC3**, **6FT-CC3**, **6ET-CC3**, and **Cocryst1**).

The practical performance of a KQS adsorbent will be a combination of its selectivity and its capacity; on this basis, the cage cocrystal shows the most promising performance.



dependent opening of the aperture allowed both H_2 and D_2 molecules to diffuse faster.

The ratio of D_2/H_2 calculated for each point on the isotherms as a function of the pressure is presented in Fig. 3C. **Cocryst1** exhibited a maximum D_2/H_2 uptake ratio of 3.5 at 30 K and 25 mbar, which is consistent with the lack of equilibrium at 30 K, implying that the cocrystal possessed good separation capabilities. To our knowledge, the D_2/H_2 uptake ratio of **Cocryst1** is one of the largest values calculated from pure-gas adsorption isotherms (6, 20, 33, 35, 36).

We investigated actual gas separation by TDS. **Cocryst1** was exposed to 10 mbar of a 1:1 H_2/D_2 mixture for 30 min at various exposure temperatures. The resulting TDS spectra for $T_{\text{exp}} = 30, 40$, and 50 K are shown in Fig. 3D; additional TDS spectra for **Cocryst1** are presented in fig. S14. The uptake after exposure to the gas mixture rose with increasing exposure temperature until a maximum for the combined gas uptake was reached at 40 K. In contrast to **6ET-RCC3**, **Cocryst1** shows desorption up to 80 K for $T_{\text{exp}} = 30$ K, indicating gas penetration of the cages at a lower exposure temperature. The uptake then decreased until no desorption peak is observed at 77 K. S_{D_2/H_2} reached a maximum of 7.7 at 30 K and dropped to lower values at 40 and 50 K (Fig. 3E). For a constant exposure temperature of 30 K, thermally activated flexibility was again observed. As exposure time increased from 10 to 600 min, S_{D_2/H_2} remained near 8.0 (7.7 to 8.2), but the D_2 uptake was enhanced from 0.4 to 4.7 mmol/g (Fig. 3, F and G), indicating hindered diffusion. X-ray diffraction data indicate that **Cocryst1** remained highly crystalline and did not change its structure during the TDS measurements (fig. S18).

The kinetics of pure H_2 and D_2 gas uptake was studied by TDS after exposure at 30 K for exposure times varying from 10 to 1200 min (fig. S14). For both gases, **Cocryst1** showed a pronounced increase in uptake for longer exposure time. Whereas the D_2 uptake was almost identical for exposure times between 600 and 1200 min, the H_2 amount still increased at longer exposure times. Because D_2 reached saturation faster, it likely had a much different diffusion rate than H_2 .

The H_2/D_2 separation properties of **Cocryst1** were excellent: $S_{D_2/H_2} \sim 8.0$, combined with a greatly enhanced D_2 uptake with respect to **6ET-RCC3** (4.7 mmol/g). The experimental S_{D_2/H_2} values for various reported porous KQS adsorbents are compared in Fig. 4 and table S3. Of these materials, only two other porous solids have combined a selectivity greater than 3 with a gas uptake larger than 1.0 mmol/g (dashed lines in Fig. 4). The cage cocrystal displays the best combination of selectivity and D_2 uptake reported to date.

Molecular simulations of the hydrogen isotope separation in organic cages

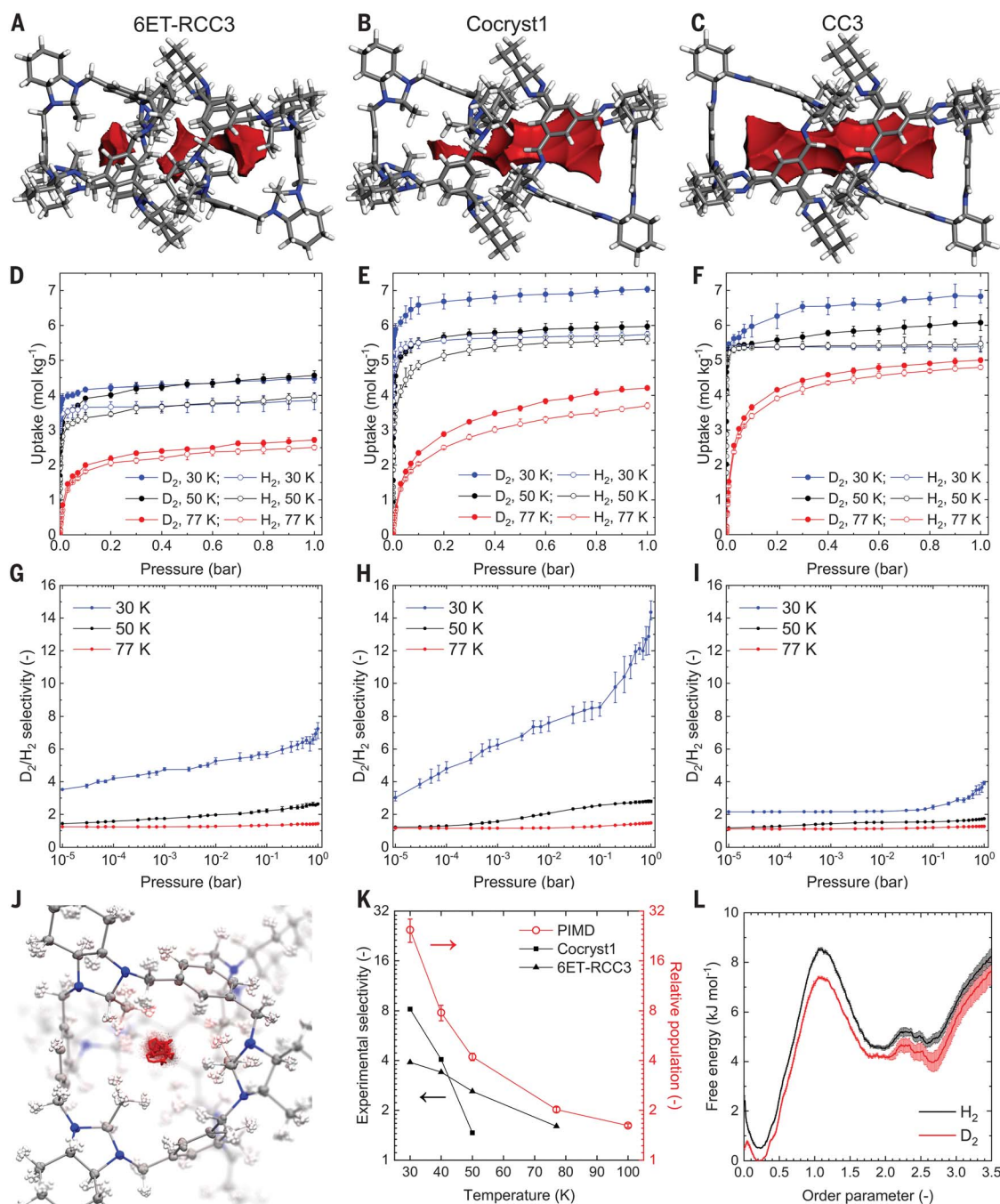
To further probe the separation mechanism, we simulated equilibrium adsorption isotherms for both single-component adsorption (Fig. 5, D to F) and an equimolar mixture of H_2 and D_2 (Fig. 5, G to I) in **CC3**, **6ET-RCC3**, and **Cocryst1** by combining grand canonical Monte Carlo (GCMC) simulations with the Feynman-Hibbs effective potential (37). We also used a hybrid GCMC-MD scheme, allowing for direct sampling of host motions in adsorption simulations, which was previously shown to be important for gas adsorption in porous organic cages (27, 38). The simulated adsorption isotherms (Fig. 5, D to I) are in good agreement with

experiment, corroborating both the experimental adsorption data and the TDS results. All three cage crystals were predicted to be selective toward D_2 over H_2 , with increased selectivity as the temperature decreases. More-

over, computation suggests, in agreement with experiment, that **Cocryst1** exhibits the high D_2 selectivity of **6ET-RCC3** and achieves the higher gas uptake capacities associated with the **CC3** partner cage.

Diffusion of the hydrogen isotopes in **CC3**, **6ET-RCC3**, and **Cocryst1** was investigated and interpreted by comparison of the free-energy barriers for H_2 and D_2 in a given crystal structure at infinite dilution (see section 2.10.3,

Fig. 5. Simulations provide insights into the mechanism for hydrogen isotope separation by the porous organic cages. (A to C) A pair of neighboring cage molecules in **6ET-RCC3** (A), **Cocryst1** (B), or **CC3** (C). Gray, white, and blue atoms represent carbon, hydrogen, and nitrogen, respectively; pore spaces inside the cage molecules, defined by a spherical probe with diameter 2.2 Å, are colored in red. In (A), the colored pore space runs through a **6ET-RCC3** cage window with two methyl groups (left cage) and a second **6ET-RCC3** cage window with one methyl group (right cage). In (B), the pore runs through a **6ET-RCC3** cage window with one methyl group (left cage) and a neighboring **CC3** cage window (right cage). (D to F) Predicted single-component adsorption isotherms of D_2 and H_2 in **6ET-RCC3** (D), **Cocryst1** (E), and **CC3** (F). Five independent simulations were performed to predict the adsorption uptake at each pressure at the respective temperature; the average of the five predicted uptakes was used to plot the isotherm, with error bars showing the maximum and minimum of the five predictions. (G to I) Predicted D_2/H_2 selectivity, calculated using competitive adsorption simulations of an equimolar D_2/H_2 mixture for **6ET-RCC3** (G), **Cocryst1** (H), and **CC3** (I). Similarly, five independent simulations were performed to predict the average uptake and to determine the error bars. (J to L) PIMD simulations predict D_2/H_2 selectivity and gas diffusion for a single, isolated **6ET-RCC3** cage (see supplementary text section 2.13 for simulation details). (J) Transition state for the translocation of a quantum H_2 molecule. A single snapshot is shown, with an overlay of all 32 replicas in the PIMD simulation, illustrating the nuclear quantum fluctuations. Additional translucent red dots depict the fluctuations of the translocating H_2 molecule, taken from 100 transition-state configurations. (K) Relative population of D_2 over H_2 inside the cage versus in the gas phase, as a function of temperature, compared with the observed experimental D_2/H_2 selectivities. (L) Free-energy profiles for a single molecule of quantum H_2 (black) or quantum D_2 (red) diffusing through a window of an isolated **6ET-RCC3** molecule at 50 K. Definitions of errors in (K) and (L) are given in section 2.13 of the supplementary text.



(J to L) PIMD simulations predict D_2/H_2 selectivity and gas diffusion for a single, isolated **6ET-RCC3** cage (see supplementary text section 2.13 for simulation details). (J) Transition state for the translocation of a quantum H_2 molecule. A single snapshot is shown, with an overlay of all 32 replicas in the PIMD simulation, illustrating the nuclear quantum fluctuations. Additional translucent red dots depict the fluctuations of the translocating H_2 molecule, taken from 100 transition-state configurations. (K) Relative population of D_2 over H_2 inside the cage versus in the gas phase, as a function of temperature, compared with the observed experimental D_2/H_2 selectivities. (L) Free-energy profiles for a single molecule of quantum H_2 (black) or quantum D_2 (red) diffusing through a window of an isolated **6ET-RCC3** molecule at 50 K. Definitions of errors in (K) and (L) are given in section 2.13 of the supplementary text.

supplementary text). In the transition-state theory approximation, molecular diffusivity can be derived from a rate constant for the molecule hopping over the free-energy barrier. Figure S31 (supplementary text) shows the free-energy profile for a diffusion pathway between the center of mass of a cage molecule and the center of mass of a neighboring cage, travelling across two cage windows. In **CC3** (fig. S31C), both H₂ and D₂ moved easily between the two cage molecules in a nearly barrier-free manner. By contrast, the congested cage cavities and narrowed window apertures in **6ET-RCC3** resulted in sharply peaked free-energy barriers (fig. S31A), strongly decreasing the molecular diffusivity compared with **CC3**.

When two methyl groups were located in a single **6ET-RCC3** cage window, the pore space became disconnected and the diffusion barrier became too large to observe any crossing (off-scale in fig. S31A; cage on the left). For windows with only one methyl group (fig. S31A, cage on the right), the pore space ran continuously between the cages, and the free-energy barriers for H₂ and D₂ were lowered substantially. Crucially, **6ET-RCC3** cage windows containing one methyl group provided diffusion barriers that were different for D₂ and H₂ and acted as a kinetic sieve. This feature was also carried over into **Cocryst1** (fig. S31B). In **Cocryst1**, the large **CC3** cavities also provided good dynamical relaxation, resulting in improved D₂ kinetics and higher D₂ uptakes.

We further combined path integral molecular dynamics (PIMD) simulations with quantum mechanical interaction evaluations to probe the adsorption and diffusion behaviors of H₂ and D₂ in the **6ET-RCC3** cage molecule, explicitly accounting for the quantum mechanical nature of both the electrons and the nuclei (Fig. 5, J to L). PIMD simulations predicted the binding free energy of D₂ to be ~0.50 kJ mol⁻¹, lower than for H₂ across the temperature range 30 to 77 K. This difference in binding free energy translates into a relative population of D₂ over H₂ inside the cage of 4.21 at 50 K (Fig. 5H), rising to 24.65 at 30 K (see section 2.13, supplementary text). There is qualitative agreement between these simulated relative populations and the measured D₂/H₂ selectivity in the temperature range 30 to 77 K (Fig. 5K). We also estimated the free-energy barriers for a single molecule of quantum H₂ and quantum D₂ diffusing out of the **6ET-RCC3** cage molecule (Fig. 5L). These simulations show that nuclear quantum effects both destabilize H₂ relative to D₂ inside the cage and also provide a higher free-energy barrier for diffusion of H₂ through the cage windows. The different barrier heights can be understood as the different degrees of zero-point fluctuations that increase the effective size of H₂ more than D₂, thereby making it more difficult for H₂ to pass through the window aperture.

Analysis of the various pore structures and the simulated adsorption and diffusion results (Fig. 5 and fig. S30) may explain why the selectivity for **Cocryst1** was double that of **6ET-RCC3** ($S_{D_2/H_2} = 8.2$ versus 3.9). The small channels in **6ET-RCC3** led to single-file diffusion. Once a molecule penetrated the pore, no passing between the isotopes in the channels is possible. Hence, the desorption after exposure to a 1:1 mixture exhibited identical maximum temperatures for both isotopes (Fig. 2C)—the gas molecules left in the same order in which they entered—whereas the maximum for pure gas desorption appeared lower for D₂ than for H₂ (Fig. 2B and fig. S7).

By contrast, **Cocryst1** consisted of a combination of large storage pores (**CC3**, also selective toward D₂ over H₂ at 30 K) and small separation pores, separated by a differential diffusional barrier (fig. S30B and Fig. 5L). Penetration through the small apertures into the adjacent larger cavity yielded an additional sieving effect, whereby D₂ molecules could pass neighboring H₂ molecules, unlike in the single-file pores of **6ET-RCC3**. As a result, **Cocryst1** had an enhanced D₂/H₂ selectivity, although there were half as many small windows as in **6ET-RCC3**.

Outlook

When researchers began to study POCs, there was a strong emphasis on producing materials with large pore volumes and high surface areas to rival solids such as MOFs (24, 39–41). Our study suggests that there are benefits in designing solids that are “barely porous” (40). By itself, this approach led to materials such as **6ET-RCC3** with low gas capacities, but by pairing small- and large-pore cages in a single cocrystal, we accessed a material with optimal gas separation properties. This strategy might be extended to produce even better performance—for example, by introducing storage cages with larger capacities than that of **CC3**, provided that the differential diffusional barrier between cages is preserved.

Our approach allows extremely delicate tuning of pore size—the entire tunability window for this series of cages spans the diameter a single nitrogen atom—and ideally suits applications such as QKS. Although the synthetic method involves multistep organic synthesis (Fig. 1B), including protection and deprotection steps, each step proceeded in nearly 100% yield. Because there was no need to purify intermediates, there is good potential to scale up the amount of materials made for practical separations.

Computational studies (Fig. 5) helped to explain the enhanced H₂/D₂ separation performance of the cocrystal. Although these calculations served to rationalize the experimental observations, the good agreement between theory and experiment suggests that the

a priori design of new systems might be possible, perhaps through methods such as crystal structure prediction to identify suitable hypothetical systems (34, 42).

REFERENCES AND NOTES

- H. K. Rae, in *Separation of Hydrogen Isotopes* (Symposium Series, ACS, 1978), vol. 68, chap. 1, pp. 1–26.
- G. M. Keyser, D. B. McConnell, N. Anyas-Weiss, P. Kirkby, in *Separation of Hydrogen Isotopes* (ACS, 1978), vol. 68, pp. 126–133.
- H. Tanaka *et al.*, *J. Low Temp. Phys.* **157**, 352–373 (2009).
- H. Oh, M. Hirscher, *Eur. J. Inorg. Chem.* **2016**, 4278–4289 (2016).
- J. J. Beenakker, V. D. Borman, S. Yu. Krylov, *Chem. Phys. Lett.* **232**, 379–382 (1995).
- J. Teufel *et al.*, *Adv. Mater.* **25**, 635–639 (2013).
- K. Adil *et al.*, *Chem. Soc. Rev.* **46**, 3402–3430 (2017).
- J.-Y. Kim, H. Oh, H.-R. Moon, *Adv. Mater.* **31**, e1805293 (2019).
- L. M. Robeson, *J. Membr. Sci.* **320**, 390–400 (2008).
- Z. R. Herm *et al.*, *Science* **340**, 960–964 (2013).
- A. Cadiau, K. Adil, P. M. Bhatt, Y. Belmabkhout, M. Eddaoudi, *Science* **353**, 137–140 (2016).
- N. B. McKeown, P. M. Budd, *Chem. Soc. Rev.* **35**, 675–683 (2006).
- P. Kowalczyk *et al.*, *J. Phys. Chem. Lett.* **6**, 3367–3372 (2015).
- G. Garberoglio, M. M. DeKlavan, J. K. Johnson, *J. Phys. Chem. B* **110**, 1733–1741 (2006).
- Q. Wang, S. R. Challa, D. S. Sholl, J. K. Johnson, *Phys. Rev. Lett.* **82**, 956–959 (1999).
- R. Xiong *et al.*, *Microporous Mesoporous Mater.* **264**, 22–27 (2018).
- M. Giraudet *et al.*, *Microporous Mesoporous Mater.* **270**, 211–219 (2018).
- H. Oh, I. Savchenko, A. Mavrandonakis, T. Heine, M. Hirscher, *ACS Nano* **8**, 761–770 (2014).
- B. Chen *et al.*, *J. Am. Chem. Soc.* **130**, 6411–6423 (2008).
- H. Oh, K.-S. Park, S. B. Kalidindi, R. A. Fischer, M. Hirscher, *J. Mater. Chem. A* **1**, 3244–3248 (2013).
- M. Lozada-Hidalgo *et al.*, *Science* **351**, 68–70 (2016).
- I. Savchenko *et al.*, *Microporous Mesoporous Mater.* **216**, 133–137 (2015).
- H. Deng *et al.*, *Science* **336**, 1018–1023 (2012).
- T. Tozawa *et al.*, *Nat. Mater.* **8**, 973–978 (2009).
- T. Hasell, A. I. Cooper, *Nat. Rev. Mater.* **1**, 16053 (2016).
- T. Mitra *et al.*, *Nat. Chem.* **5**, 276–281 (2013).
- L. Chen *et al.*, *Nat. Mater.* **13**, 954–960 (2014).
- M. W. Schneider, I. M. Oppel, A. Griffin, M. Mastalerz, *Angew. Chem. Int. Ed.* **52**, 3611–3615 (2013).
- M. Liu *et al.*, *J. Am. Chem. Soc.* **136**, 7583–7586 (2014).
- T. Hasell *et al.*, *J. Am. Chem. Soc.* **136**, 1438–1448 (2014).
- D. Banerjee *et al.*, *Acc. Chem. Res.* **48**, 211–219 (2015).
- C. A. Fernandez, J. Liu, P. K. Thallapally, D. M. Strachan, *J. Am. Chem. Soc.* **134**, 9046–9049 (2012).
- D. Noguchi *et al.*, *J. Am. Chem. Soc.* **130**, 6367–6372 (2008).
- J. T. A. Jones *et al.*, *Nature* **474**, 367–371 (2011).
- S. A. FitzGerald, C. J. Pierce, J. L. C. Rowsell, E. D. Bloch, J. A. Mason, *J. Am. Chem. Soc.* **135**, 9458–9464 (2013).
- B. Xiao *et al.*, *J. Am. Chem. Soc.* **129**, 1203–1209 (2007).
- L. M. Sesé, *Mol. Phys.* **85**, 931–947 (1995).
- S. Yang *et al.*, *Kristallogr. Cryst. Mater.* **234**, 547–555 (2019).
- M. Mastalerz, M. W. Schneider, I. M. Oppel, O. Presly, *Angew. Chem. Int. Ed.* **50**, 1046–1051 (2011).
- A. I. Cooper, *Angew. Chem. Int. Ed.* **51**, 7892–7894 (2012).
- G. Zhang, O. Presly, F. White, I. M. Oppel, M. Mastalerz, *Angew. Chem. Int. Ed.* **53**, 1516–1520 (2014).
- A. Pulido *et al.*, *Nature* **543**, 657–664 (2017).
- G. J. Kleywegt, T. A. Jones, *Acta Crystallogr. D* **50**, 178–185 (1994).
- J. Teufel, “Experimental investigation of H₂/D₂ isotope separation by cryo-adsorption in metal-organic frameworks,” thesis, Universität Stuttgart (2013).
- S. S. Mondal *et al.*, *ChemPhysChem* **20**, 1311–1315 (2019).
- H. Oh *et al.*, *Angew. Chem. Int. Ed.* **52**, 13219–13222 (2013).

ACKNOWLEDGMENTS

We thank Diamond Light Source for access to beamlines I19 (CY21726) and I11 (EE17193). We thank the Advanced Light Source, supported by the Director, Office of Science, Office of Basic Energy Sciences, of the U.S. Department of Energy under contract no. DE-AC02-05CH11231 and also thank S. J. Teat for his assistance during this experiment. We thank M. Wang (University of Liverpool) for computing facilities support and A. Hill (Department of

Chemical Engineering, University of Bath) for discussions on the practicability of using cage materials for hydrogen isotope separation. **Funding:** We gratefully acknowledge the Engineering and Physical Sciences Research Council (EP/N004884/1), the European Research Council under the European Union's Seventh Framework Programme (FP/2007-2013)/ERC through grant agreement no. 321156 (ERC-AG-PE5-ROBOT), and the Leverhulme Trust via the Leverhulme Research Centre for Functional Materials Design for funding. S.Y. and L.D. acknowledge financial support from the Chinese Young Scholar National Science Foundation Grant (21403171), the Xi'an JiaoTong-Liverpool University (XJTLU) Research Development Fund (PGRS-13-03-08), and the Key Program Special Fund in XJTLU (KSF-E-03). D.H. thanks the Oversea Study Program of Guangzhou Elite Project from Guangzhou City, China, for financial support. V.K. and M.C. acknowledge funding from the Swiss National Science Foundation (project ID 200021-159896) and the European Research Council

under the European Union's Horizon 2020 research and innovation program (grant agreement no. 677013-HBMAP). **Author contributions:** M.L., L.C., and A.I.C. conceived the project. M.L. and D.H. synthesized and characterized the materials. L.C. conceived the modeling strategy and supervised the computational work, with input from L.D. and M.C. L.C., S.Y., and D.L.H. performed the classical simulations. V.K., L.C., and M.C. performed the electronic-structure, PIMD, and free-energy simulations. M.A.L. supervised the structural part of this study and refined all diffraction data. M.L. and M.A.L. cultured single crystals and performed solid-state crystal synthesis. M.A.L. and S.Y.C. carried out powder x-ray diffraction analyses. R.C. collected gas sorption data. M.H. and G.S. conceived the hydrogen isotope separation measurements. L.Z. and R.B.-X. collected the H_2 and D_2 isotherms. L.Z. performed TDS experiments. L.Z. and M.H. interpreted the TDS data. All authors contributed to the writing of the paper. **Competing interests:** The authors declare no competing interests.

Data and materials availability: The crystallographic data reported in this paper are listed in the supplementary materials and archived at the Cambridge Crystallographic Data Centre under reference numbers CCDC 1910113 to 1910120. All other data needed to evaluate the conclusions in the paper are present in the paper or the supplementary materials.

SUPPLEMENTARY MATERIALS

science.sciencemag.org/content/366/6465/613/suppl/DC1
Materials and Methods
Supplementary Text
Figs. S1 to S44
Tables S1 to S8
References (47–95)

18 April 2019; accepted 10 October 2019
10.1126/science.aax7427